



Article

Device Modeling of Organic Photovoltaic Cells with Traditional and Inverted Cells Using s-SWCNT:C₆₀ as Active Layer

Vijai M. Moorthy * and Viranjay M. Srivastava

Department of Electronic Engineering, Howard College, University of KwaZulu-Natal, Durban 4041, South Africa
* Correspondence: vijaimyappan@gmail.com

Abstract: This research work presents a thorough analysis of Traditional Organic Solar Cell (TOSC) and novel designed Inverted OSC (IOSC) using Bulk Hetero-Junction (BHJ) structure. Herein, 2D photovoltaic device models were used to observe the results of the semiconducting Single Wall Carbon Nanotube (s-SWCNT):C₆₀-based organic photovoltaic. This work has improved the BHJ photodiodes by varying the active layer thickness. The analysis has been performed at various active layer thicknesses from 50 to 300 nm using the active material s-SWCNT:C₆₀. An analysis with various parameters to determine the most effective parameters for organic photovoltaic performance has been conducted. As a result, it has been established that IOSC has the maximum efficiency of 10.4%, which is higher than the efficiency of TOSC (9.5%). In addition, the active layer with the highest efficacy has been recorded using this material for both TOSC and IOSC Nano Photodiodes (NPDs). Furthermore, the diode structure and geometrical parameters have been optimized and compared to maximize the performance of photodiodes.

Keywords: carbon nanotube (CNT); bulk hetero-junction structure; device modeling; organic solar cells; inverted organic solar cells; microelectronics; nanotechnology; VLSI



Citation: Moorthy, V.M.; Srivastava, V.M. Device Modeling of Organic Photovoltaic Cells with Traditional and Inverted Cells Using s-SWCNT:C₆₀ as Active Layer. *Nanomaterials* **2022**, *12*, 2844. <https://doi.org/10.3390/nano12162844>

Academic Editor: Guanying Chen

Received: 19 July 2022

Accepted: 11 August 2022

Published: 18 August 2022

Publisher's Note: MDPI stays neutral with regard to jurisdictional claims in published maps and institutional affiliations.



Copyright: © 2022 by the authors. Licensee MDPI, Basel, Switzerland. This article is an open access article distributed under the terms and conditions of the Creative Commons Attribution (CC BY) license (<https://creativecommons.org/licenses/by/4.0/>).

1. Introduction

Solar energy has achieved various advancements due to renewable energy sources in the last few decades. These devices provide long-term power at a low operating cost and low pollution. The photovoltaic effect is the underlying principle of this technology. When exposed to sunlight, solar cells convert that energy into electrical current. Based on the material configuration, organic cells are classified as third-generation solar cells [1]. Since their discovery over a decade ago, organic photovoltaic devices have attracted considerable attention as non-conservative renewable energy sources [2,3]. In 1960, Williams [4] had performed an experimental analysis on photovoltaic effects that occur at semiconductor electrolyte interfaces. The cadmium sulfide and various other compounds were studied using single-crystal specimens. The analysis exposes the photovoltaic effects of electrode materials when they chemically react with one another. Loferski [5] explained that the advances in quantum mechanics and semiconductor technology enabled a deeper understanding of photovoltaic effects and resulted in the creation of more advanced photovoltaic devices.

Goetzberger et al. [6] have reported that selenium solar cells have less than 1% conversion efficiency. Therefore, experiments were carried out on a variety of other materials, in which the majority met these criteria; however, the most effective photovoltaic devices used p–n junctions on silicon semiconductor materials [7]. The first solid-state solar cell was used in 1883 by coating a thin gold film over a selenium semiconductor to form a junction. Ohl [8] have analyzed a crystalline silicon sample with a crack in the middle that formed an electric current when exposed to light. This work paved the way for silicon PV technology, which is a Si p–n homojunction cell with top and bottom electrodes. A typical Si solar cell starts with a p-type substrate that was doped to form an n-type emitter on top. Then, phosphorus is diffused into the base substrate during n-type doping and screen

printing creates the top and bottom electrodes. Printing solar cells is the simplest and most established way of producing them. Moreover, to enhance the device's performance, the top surface of the cell has been coated with an anti-reflection coating.

Alferov [9] has reported that solar cells with p–n junctions are composed of Aluminum Gallium Arsenide and Gallium Arsenide (GaAs) hetero-junctions. The GaAs solar cells had only one flaw: They were expensive to produce. The Czochralski and the Bridgman methods were initially used to produce single crystals of GaAs. Due to the low efficiencies and imperfect crystals, these methods for material growth were not successful. Their threshold current densities have been achieved at $(4\sim 5) \times 10^3$ A/cm² at 300 K. Organic semiconductor-based OSCs are solid-state thin-film solar cells. Organic semiconductors are aromatic hydrocarbons with sp² hybridized carbon atoms that have alternate single and double bonds, such as a semiconductor. These materials are known as conjugated semiconductors due to the change in single and double bonds between carbon atoms. According to Chen et al. [10], the conjugated polymers based on organic semiconductors are a substitute for inorganic devices due to their various favorable characteristics, including portability, adaptability, and solution process deposition at ambient temperature. The highest external quantum efficiency observed for the OSC BHJ solar cell was 0.836 for 500 nm wavelength and 0.815 for 450 nm IOSB BHJ solar cell.

Furthermore, Malti et al. [11] have claimed that solar energy efficiency improved through a number of initiatives. The device-level efficiency of white light has been improved to 5%. A maximum efficiency of around 8% is achieved when the band-gap of the cell is around 1.5 eV, $V_{oc} = 0.61$, for 400 nm thickness at $T = 300$ K. Brabec et al. [12] have reported results contrary to inorganic technologies, which have higher efficiency. The ability to produce Organic Photo Voltaic (OPV) on low-cost substrates in reel-to-reel fashion with regular coating and printing methods is the primary characteristic that makes OPV significantly attractive. The OPV was discussed in terms of economic and technological aspects of manufacture. Yu et al. [13] have fabricated the OSC using C₆₀ and its functionalized derivatives were used to mix with the semiconducting polymer. Herein, two orders of magnitude better than those that have been achieved by pure MEH-PPV devices were observed, due to the remarkable efficiencies of the materials used. As a result, significant efforts have been exerted to enhance the efficiency of OSCs by employing cutting-edge materials and designs, etc. This aim was achieved by $h_c = 90\%$ and $h_e = 5.5\%$ at 10 mW/cm² for internal carrier collection efficiency and energy conversion efficiency.

Scharber and Sariciftci [14] have examined the BHJ solar cells and their basic principles of operation and device design. The commercial viability of BHJ solar cells depends on their ability to convert solar energy into electrical energy with high efficiency. The Power Conversion Efficiency (PCE) in the range of 10–15% was predicted by several models based on the best available materials and device architectures. Higher efficiencies were achieved if the Shockley–Queisser limit was considered. Inorganic photovoltaic systems that depend only on charge carrier recombination by radiation may be as efficient as BHJ devices that do not show this phenomenon. Marinova et al. [15] have presented an overview of the key processes in photovoltaic systems based on OSCs and Perovskite Solar Cells (PSCs), focusing on interfacial processes of engineering materials. Recently, the authors have employed poly (3-hexylthiophene-2, 5-diyl):phenyl-C61-butyric acid methyl ester (P3HT:PCBM) blends in polymer solar cells. A transparent conductive electrode material used in BHJ is Indium Tin Oxide (ITO). BHJ may be classified into two types: Traditional and inverted.

At a later time, Kumavat et al. [16] reported the development of solar cells, including some fundamental concepts used in Dye-Sensitized Solar Cells (DSSCs) and OSCs. The OSCs and DSSCs are two of the technologies mentioned in the review. Liang et al. [17] have examined the impact of Zinc Oxide (ZnO) surface modification, Common Buffer Layer (CBL) shape, composition/hybrids, thickness, nanostructures, and doping on the efficacy of inverted PSCs. This research assisted in the acquisition of further knowledge on the subject. The authors reviewed the most extensively used CBL, which is produced

from pristine ZnO for improving PCE and long-term device stability. For high PCE in inverted PSCs, using a high-quality CBL material that allows for efficient electron collection and transport is critical. This is due to its excellent electron mobility, optical transparency, low-cost solution methods at low temperatures, a wide range of morphologies, and its environmental stability. ZnO material has been widely examined for CBL of inverted PSC. As established in this work, electronic processes occurring at the interface between the ZnO CBL and the active polymer layer considerably impact solar cell performance.

According to a subsequent publication, Zhao et al. [18] have stated that the IOSC based on active layer P3HT:PCBM material was composed of a Molybdenum Trioxide (MoO_3) Hole-Transporting Layer (HTL) and very thin Calcium (Ca) Electron-Transporting Layer (ETL). Additionally, the cell was capable of working at high temperatures. Adding 1 nm of Ca to an ITO electrode changes the ITO work function, rendering it better suited to the extraction of electrons, with an achievement of 3.55% PCE. Zhao et al. [19] have designed an IOSC with an extremely thin Ca layer for electron transport, a photon-absorbing combination of P3HT and PCBM, and a performance-optimized MoO_3 layer enabling hole transport. A MoO_3 layer was inserted between the anode and active layer. According to the findings of the research, this increased the performance of the device significantly, with an achievement of 3.86% PCE for the optimized device. Waldauf et al. [20] have produced an effective electron selective bottom contact by covering ITO with solution-processed Titanium Oxide (TiO_x), and then annealing the resulting structure. As an efficient carrier collecting network with low vertical phase segregation, o-xylene is employed in both conventional and IOSC applications. With the application of o-xylene, a carrier network was created, which is highly hygroscopic and transparent to light. These inverted layer sequence OPVs have PCE of more than 3%.

However, White et al. [21] have created an OSC, which is composed of ITO electrode with a P3HT/fullerene combination and a solution-processed ZnO interlayer between ITO and the active layer, with Silver (Ag) functioning as a hole-collecting back contact. When electron extraction by ZnO and hole extraction via Ag are both successful, with little open-circuit potential loss, a PCE of 2.58% was observed, along with minimum loss in open-circuit potential. Gilot et al. [22] have compared theoretical calculations using optical modeling to real findings for systems using ZnO as an optical spacer. The P3HT and PCBM mix showed good agreement. Another issue with organic materials is their weak absorption, which is primarily restricted to the visible range. Behjat et al. [23] have discovered that utilizing a ZnO layer as an optical spacer between the active layer and reflecting electrode allows the optical electric field (present within BHJ solar cells) to be re-distributed within the solar cell structure. ZnO film can be transmitted into the absorbing layer (the maximum level of the electric field) according to the theoretical analysis carried out using optical modeling. An optical spacer was used in this work to compare theoretical calculations to practical results. A substantial improvement in short-circuit current density was observed when a ZnO optical spacer layer was utilized. The PCE of the BHJ solar cell was increased by up to 3.49% due to the device's electrical and optical properties.

Lee et al. [24] have demonstrated that TiO_x may be used as an optical spacer in the BHJ structure. The findings showed that the TiO_x optical spacer's improved efficiency is inversely related to the amount of processing additive used. Surface roughness is produced on the BHJ film as a result of the manufacturing process, which reduces the efficiency of the optical spacer. Alternatively, active layer nanomaterials, such as CNTs and fullerene derivatives can be used to produce an efficient NPD.

Yang et al. [25] recently demonstrated that N,N-di(2-ethylhexyl)-6,6'-dibromoisindigo and an amino-containing fluorene subunit were effectively combined to form the alcohol-soluble polymer PFN-ID for OSC using PTB7-Th:PC71BM as the active layer. The optimal PCE of 9.24% is achieved, which is 1.62 times greater than the devices without cathode interfacial layers. Xue et al. [26] employed the Methyl Salicylate (MeSA) in their study as a non-halogen additive for inverted OSCs, and its effects on the performance of the blend film and photovoltaic system were analyzed. The findings show that MeSA exhibits

an efficiency of 9.45% and improved FF (>70%) with a 7% MeSA additive. Ren et al. [27] employed Tetrasodium Iminodisuccina (IDS), which is a non-conjugated small molecule added to the conventional devices based on PTB7-Th:PC71BM to serve as an Electron Transport Layer (ETL). The PCE of 9.45% is achieved with V_{oc} of 0.80 and FF of 70.01%.

In the previous research work, Moorthy et al. [28–30] have analyzed the BHJ and Planar Hetero-Junction (PHJ) topologies utilizing various nanomaterials and fabricating and testing the NPD device for the subretinal implant. The nanomaterials used improved the BHJ performance for the subretinal implant application.

To extend the author's previous work [28–30], this present research work realizes the novel model of TOSC and IOSC BHJ. The authors analyzed the performance of both the TOSC and IOSC NPD cells using organic materials and device architecture on cell performance for various configurations with various light-absorbing materials and thin sheets to optimize the cell's hole and electron transport layers. Molecular structures of s-SWCNT and C_{60} perform better than the other active layer's blends, as reported in the authors' previous work. An organic photovoltaic cell based on a single diode cell has been used in this work.

This research work has been organized as follows: Section 2 presents the structure of the proposed photovoltaic devices, as well as the selection of active layer, ETL, HTL, and electrode materials. Section 3 discusses the methodology of PV cell structures, which is comprised of organic semiconductors, such as conjugated polymers (CP), as active materials and transparent electrodes. Section 4 provides a comparison, optimization, and evaluation of TOSC and IOSC NPD structures. Finally, Section 5 concludes our work and provides recommendations for future work.

2. Structures of TOSC and IOSC Organic Nano Photodiodes and Choice of Materials

To conduct this research, a passive OPV device has been used to transform light intensity into an electric current. Figure 1 shows the OSC fundamental structure. One of the primary goals of this research is to examine and compare how the TOSC and IOSC device architectures affect the performance of the device, depending on material properties and layer thickness. The second goal is to optimize the design to achieve maximum performance.

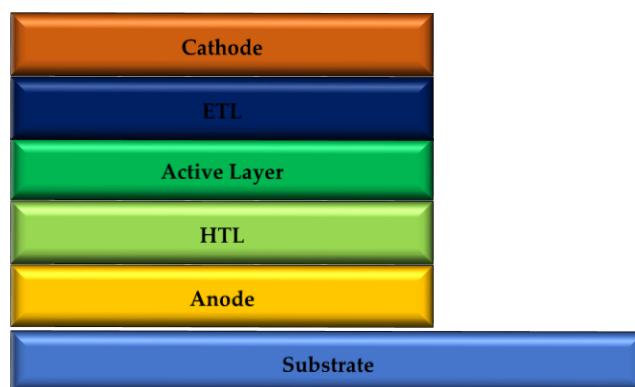


Figure 1. Structure of the TOSC.

TOSC and IOSC NPD Structure Using BHJ

A polymer, CNT, ITO, PEDOT:PSS, and aluminum materials are all used to design the TOSC and IOSC NPD structures. These NPD structures generate power under incident light. This section presents the structures of the proposed photovoltaic devices to be examined in this work and the selection of active layer, HTL, ETL, and electrode materials. The reasons underlying this choice of materials are as follows:

- A. In this model, the ITO material has been used as a transparent electrode due to its various features. In the author's previous works [28–30], graphene has been utilized as an electrode due to its biocompatibility and unique properties that suit the subretinal

implant application. However, there were some shortcomings while fabricating the graphene-based OSC. Therefore, in this present analysis, the authors employ the ITO due to its electrical conductivity, optical transparency, simplicity of deposition as a thin layer, and chemical resistance to moisture. The film's conductivity improves with thickness and charge carrier concentration, while its transparency diminishes. For applications demanding low-cost, large-area manufacturing, ITO is an attractive solution [31,32].

- B. The PEDOT:PSS layer is commonly employed as an HTL in both OSC and DSSC. This is due to the fact that it smoothens the ITO electrode surface, which is critical in OSC and DSSC. Additionally, due to its strong electrical conductivity and excellent oxidation resistance, it is well suited for electromagnetic shielding and noise suppression applications. In the visible, near-infrared, and ultraviolet light spectrums, PEDOT:PSS-based polymeric films exhibit excellent transparency, with almost 100% absorption from 900 to 2000 nm. Moreover, they are transparent in the near-infrared and near-ultraviolet regions. However, PEDOT offers the conduction properties, and PSS (in contact with water) results in the formation of a hydrated colloidal solution [33].
- C. The s-SWCNTs provide a unique combination of the solution processability, electrical tunability, and robust absorption of organic semiconductors with high charge mobilities, as well as outstanding chemical stability. Since they are strong optical absorbers with adjustable band-gaps, transfer energy and charge on ultrafast timescales are reasonably chemically stable. Additionally, solution-processable s-SWCNTs are attractive photo absorbers for next-generation photovoltaic solar cells and photodetectors. Due to these characteristics, s-SWCNT is the ideal donor material for this research [34,35].
- D. Fullerene (C_{60}) or C_{60} is composed of 60 carbons, with 20 hexagonal and 12 pentagonal sections. Fullerene does not have a saturated state. Three carbons are linked together rather than four by the fused rings of carbons 5 and 6, so-called carbon 60 fullerenes. Fullerene is a molecule that can accept electrons. Depending on their properties, it can be employed in thermal evaporation systems as electron acceptors. Moreover, it can be used as an interface layer. C_{60} fullerene can be better as an electron acceptor since it is more compatible and can deliver suitable composites with the donor material [36].
- E. One of the most common ETLs in PSCs and OSCs is Titanium Dioxide (TiO_2). It is one of the widely utilized ETLs since it is very good at transmitting light in the visible range [37].
- F. The work function of the cathode material should be lower than the anode material. The work function of aluminum is 4.2 eV, which is smaller than the ITO work function of 5.1 eV, and thus meets the criteria.

The BHJ sandwiched between the ETL and HTL is a blend of donor and acceptor with discrete band gaps. The ITO and aluminum electrodes are two layers that play a role in the process of exciton generation, diffusion, and free-carrier generation processes. Detailed representations of the TOSC and IOSC BHJ structures considered in this work are shown in Figure 2a,b, respectively, along with the materials and layer thicknesses used in each structure.

Figure 2a depicts the TOSC NPD based on the BHJ structural configuration. Aluminum metal is used as the cathode, TiO_x is used as the ETL, the electron donor is s-SWCNT, while the electron acceptor is C_{60} fullerene, since an HTL PSS is utilized and ITO is used as the anode. The BHJ-based TOSC is defined by sandwiching a blend of donor and acceptor between the ETL and HTL to form a junction. This limits the photoactive layer thickness and consequently the absorption effectiveness. The BHJ concept overcomes the PHJ device's exciton diffusion barrier. Donor and acceptor materials are completely mixed in polymer BHJ. To achieve 100% efficiency in exciton separation, the mixed layer has created a donor-acceptor interface that is spatially distributed.

The TOSC BHJ solar cell is composed of the same materials as the IOSC NPD, with the exception that the ETL and HTL layers have been switched. Figure 2b depicts the IOSC BHJ NPD structure that has been realized in this research. Moreover, the TOSC

structure is composed of the cathode aluminum metal, TiO_x as ETL, electron donor s-SWCNT, electron acceptor C₆₀ fullerene, PEDOT:PSS as HTL, and ITO as the anode. These materials are produced on a flexible/glass substrate, which improves the efficiency and transparency of the device by increasing its transparency. The structure is used for TOSC substrate/ITO/PEDOT:PSS (HTL)/s-SWCNT:C₆₀ (blended active layer)/TiO_x (ETL)/Al. For IOSC, the structure is inverted by swapping the HTL PEDOT:PSS and ETL TiO_x. The IOSC is organized as follows: Substrate/ITO/TiO_x (ETL)/s-SWCNT:C₆₀ (blended active layer)/PEDOT:PSS (HTL)/Al. Each OSC and IOSC cell has two lighted sides, which are both placed on one side of the transparent ITO substrate. The existence of ETL and HTL collects electrons and holes at their respective electrodes and transports them to their corresponding destinations. The thickness of the different active layers has been explored in detail and contrasted between the two structures.

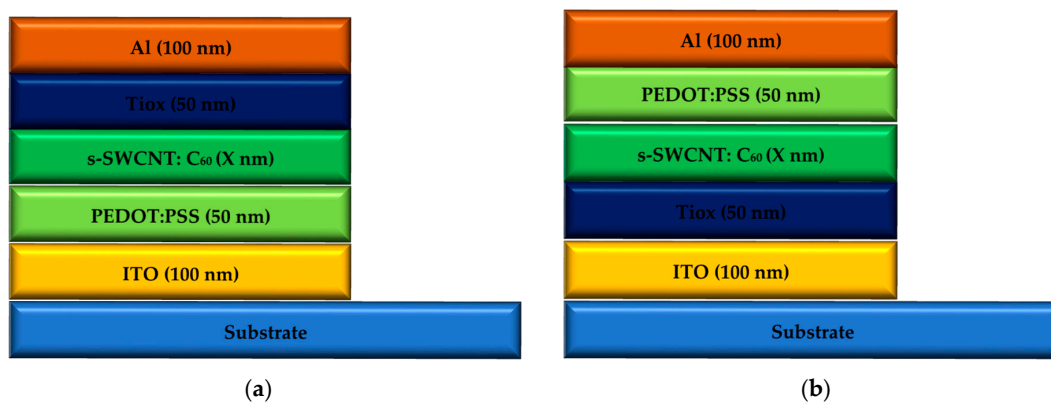


Figure 2. (a) Proposed TOSC and (b) IOSC structure.

The purpose of this research is to design, analyze, compare, and contrast the TOSC and IOSC NPDs using BHJ structures. Various physical characteristics, such as the thicknesses of different layers and other factors, have been used to develop this structure. To determine the I–V characteristics of these NPDs, an electronic device simulator has been used. In this instance, the anode contact is supplied with a bias voltage; the voltage range is 0.01 to 0.09 V, with a 0.05 V step increase.

3. Device Design Methodology

To represent the charge carrier transit in the device, the model is used to determine all electrons, carrier continuity, and drift-diffusion hole equations in location space, which is a location space representation of the device. In addition, the model determines Poisson's equation to estimate the electrostatic potential. The SRH formalism, established by Shockley–Read–Hall has been utilized to describe carrier trapping and recombination in the model [38]. Model parameters may be used to control the distribution of trap states, which allows for a more realistic representation of recombination and carrier trapping [39–41]. Organic semiconductors' opto-electronic transport method relies on the Density Of States (DOS) due to their amorphous nature [42–44]. For transport and carrier trapping, this tool makes use of the finite-difference drift-diffusion model, which is based on finite differences.

To estimate the free-carrier transport, the BHJ material is treated as a single layer, with the band-gap energy defined by the *p*-type HOMO (highest occupied molecular orbital) and *n*-type LUMO (lowest unoccupied molecular orbital) energies [21]. In the organic materials, the HOMO level corresponds to the E_v energy band-gap edge, whereas the LUMO corresponds to the E_c energy band gap edge. Since the BHJ is a combination of *n*-type and *p*-type zones, the most straightforward approach is to represent it as an analogous layer with an equivalent band-gap energy between the *p*-type HOMO and *n*-type LUMO levels. The following are the basic equations employed in this model [38–42]:

Gauss's Law:

$$\nabla \cdot \epsilon_0 \epsilon_r \nabla \phi = q(n - p) \quad (1)$$

where q is the elementary charge on an electron, ϵ_0 and ϵ_r denote the permittivity of free space and the relative permittivity of the active layer, respectively, n and p are the free electron and hole densities, respectively. For electrons and holes, the bi-polar drift-diffusion equations are solved in position space. These equations are solved to obtain the electron current flux density J_n and the hole current flux density J_p :

$$J_n = q\mu_e n \nabla E_c + qD_n \nabla n \quad (2)$$

$$J_p = q\mu_h p \nabla E_v - qD_p \nabla p \quad (3)$$

where J_n and J_p represent the electron current flux density J_n and the hole current flux density J_p . Here, the Maxwell–Boltzmann statistics for the free carriers are assumed, where D_n ; p denote the electron and hole diffusion coefficients.

To achieve this, it is necessary to conserve charge carriers by solving the charge carrier continuity equations for electrons and holes, which are illustrated in Equations (2)–(5), respectively. Electron continuity equation:

$$\nabla \cdot J_n = q \left(R - G + \frac{\partial n}{\partial t} \right) \quad (4)$$

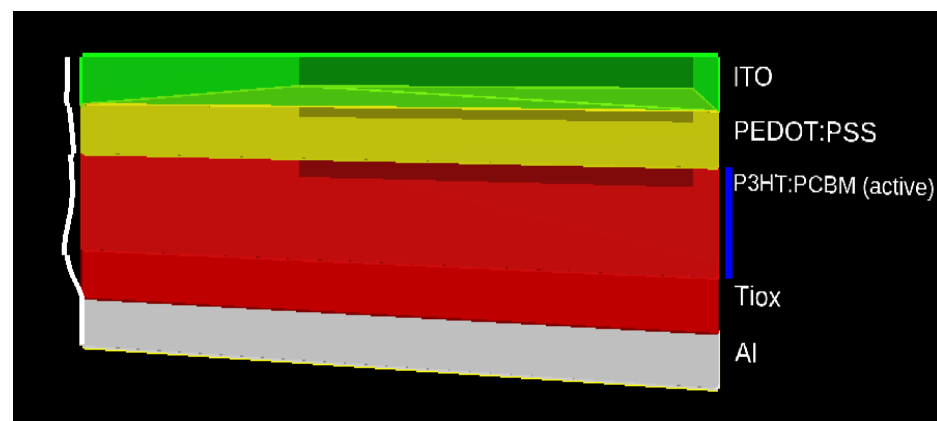
Hole continuity Equation:

$$\nabla J_p = -q \left(R - G + \frac{\partial p}{\partial t} \right) \quad (5)$$

where R and G represent the net recombination and generation rates per unit volume, respectively.

The above equations are used to model the proposed structures, which are created using the simulation tool by defining thicknesses of different layers and other physical characteristics. The simulations are carried out to obtain the J-V characteristics. At a temperature of 300 °C, numerical simulations of TOSC and IOSC were performed using the AM1.5 spectra. In this simulation model, the Neumann boundary condition with four electrical and six excitonic boundary conditions is utilized. The parameters obtained from the J–V characteristics are the current density-voltage characteristics (J-V), which include the short-circuit current density (J_{sc}), open-circuit voltage (V_{oc}), fill factor (FF), and efficiency (η).

Figure 3a,b depicts the NPD structure of TOSC and IOSC utilizing the BHJ structure, respectively. Figure 3a shows the organic solar cell structure (substrate/IITO/PEDOT:PSS/s-SWCNT:C₆₀ (blended active layer)/TiOx/Al), which is a distinctive structure in which the cell is composed of an absorber layer (s-SWCNT:C₆₀) and a hole transport layer (PEDOT:PSS). This assists the absorber layer in transporting charge carriers into an electron.



(a)

Figure 3. Cont.

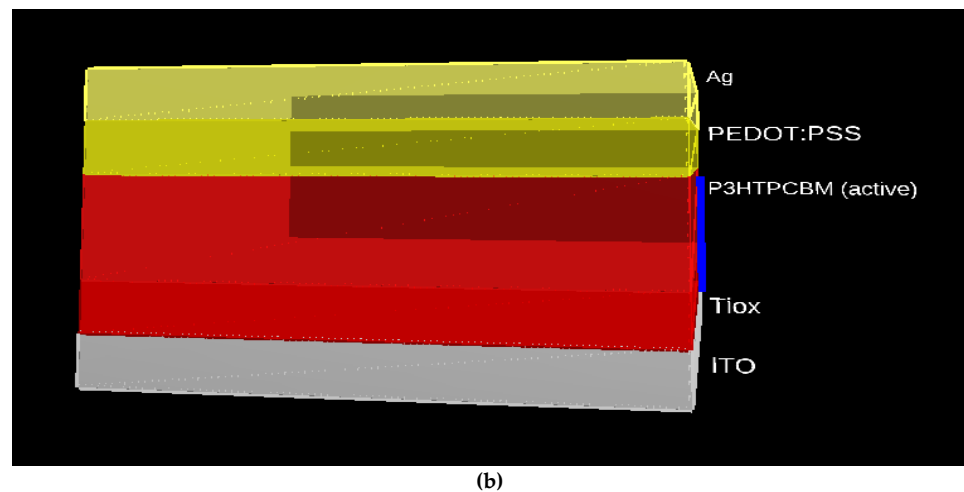


Figure 3. (a) TOSC and (b) IOSC BHJ structures used in this work.

4. Results and Analysis

This work has demonstrated the hybrid architecture of TOSC and IOSC organic photodiode cells, which is composed of nanomaterials. This architecture allows them to optimize the different geometries of the devices and compare their outputs. To improve the performance of NPD devices, the TOSC and IOSC NPD cells with BHJ structures have been modeled. The results obtained have been compared to determine which structures have the best performance.

The properties of each solar cell have a role in increasing its PCE. The V_{oc} is the difference in energy level between the potentials in the regions where free electrons and free holes predominate. The second parameter is J_{sc} , the number of photogenerated carriers formed in the active layer upon illumination and the effectiveness of charge separation across the photoactive layer determines J_{sc} [43,44]. As a result, to alter J_{sc} , one needs to vary the structure that results in the lowest useable band-gap or alter the thickness of the active layer. The FF is the ratio of the maximum electrical power produced by the cell to the product $J_{sc} \times V_{oc}$. The FF influences the cell quality and corresponds to the V_{oc} , J_{sc} , and the shape of the active layer. The PCE is defined as the product of V_{oc} , J_{sc} , and FF . The relationship between cell electrical power and incident light power is represented by this measure [45,46].

The electrical device simulator has been used to mimic organic photodiode cells' TOSC and IOSC architectures. The primary goal of these models is to optimize the anode layer thickness, active layer thickness, and cathode layer thickness to achieve the highest possible photocurrent density, the highest possible photovoltage, and efficiency. Consequently, the TOSC and IOSC device designs depicted in Figure 3 have been designed for simulation tests and the effects of various layer geometries on the above-mentioned device performance characteristics. The findings acquired for different structures have been compared to determine the optimal device dimensions for the device that provides the best overall performance.

4.1. Effect of Active Layer Thickness Variation

Optics, such as reflections at layer interfaces and accompanying interferences, cause complex enhancing difficulties that are proportional to the active layer thickness in the BHJ device. It is critical to analyze the active layer thickness since it affects light absorption and, consequently, the formation of excitons inside the active layer. In the BHJ device, layers are layered successively on top of one another, and optical events, such as reflections at layer interfaces and associated interferences, produce a complicated enhancing problem proportional to the active layer thickness [47]. The influence of active layer thickness on several parameters, such as V_{oc} , J_{sc} , FF , and η , has been evaluated and plotted against the thickness of the active layer for both TOSC and IOSC devices.

To conduct a comparative analysis and improve each BHJ structure's performance, the active layer thickness varied from 50 to 300 nm. The author addresses organic photodiodes, in which the active layer thickness is changed between 50 and 300 nm. The anode layer 100 nm, HTL layer 50 nm, ETL layer 50 nm, and the cathode layer 100 nm remained constant. Figure 4 illustrates the comparison plot characteristics of TOSC (solid lines) and IOSC (dashed lines) for various active layer thicknesses from the JVV curves. The J_{sc} characteristics are shown to be quite sensitive to changes in the active layer thickness. As previously stated, the J_{sc} is significantly correlated with the active layer's absorption. In both TOSC and IOSC, the thickness of the active layer has a considerable effect on J_{sc} , η , and FF , while V_{oc} appears to be less sensitive, as seen in Figure 4. Both the absorption and the diffusion length have an effect on the carrier photogeneration and transport as reflected by the J_{sc} parameter.

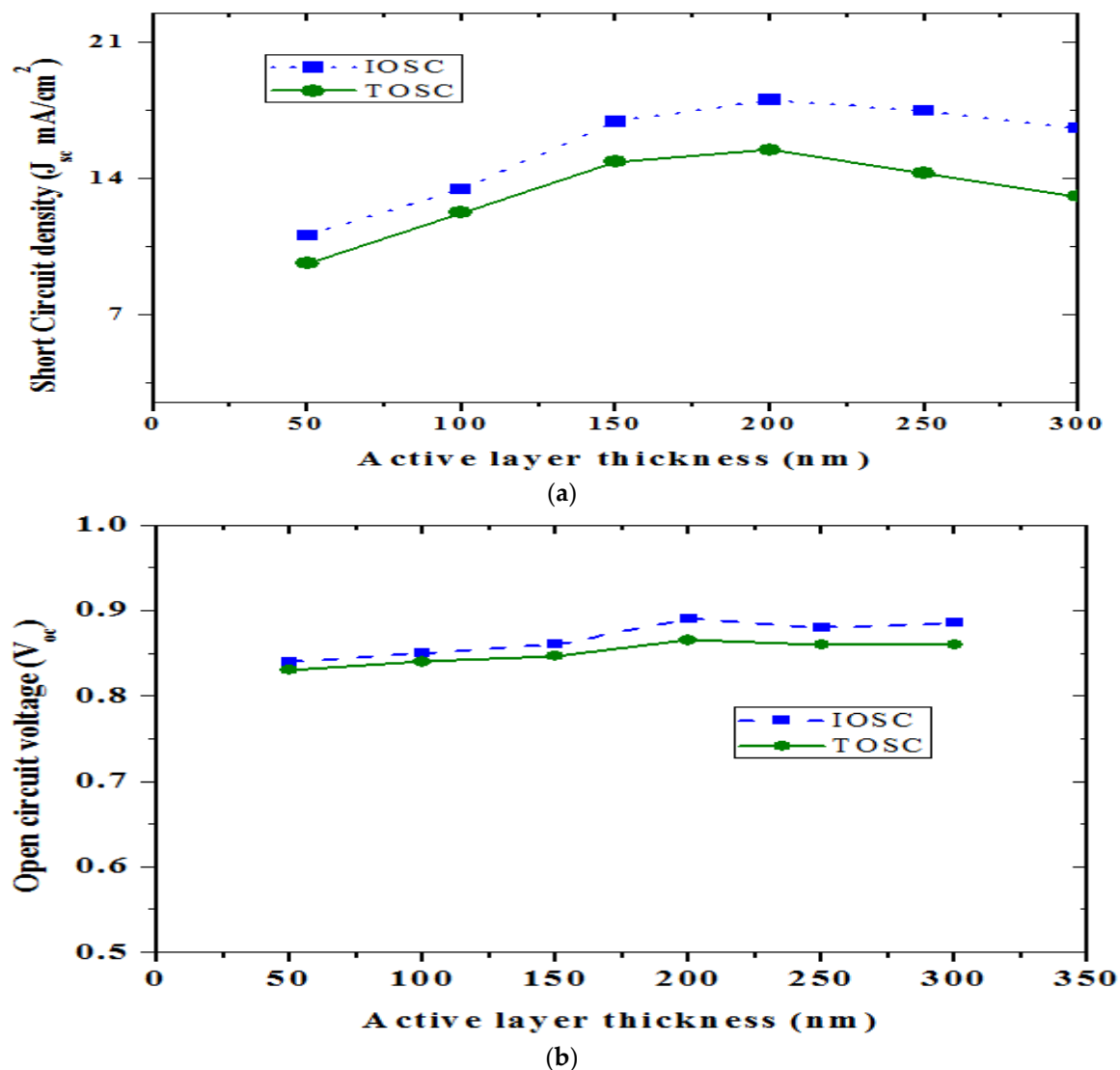


Figure 4. Cont.

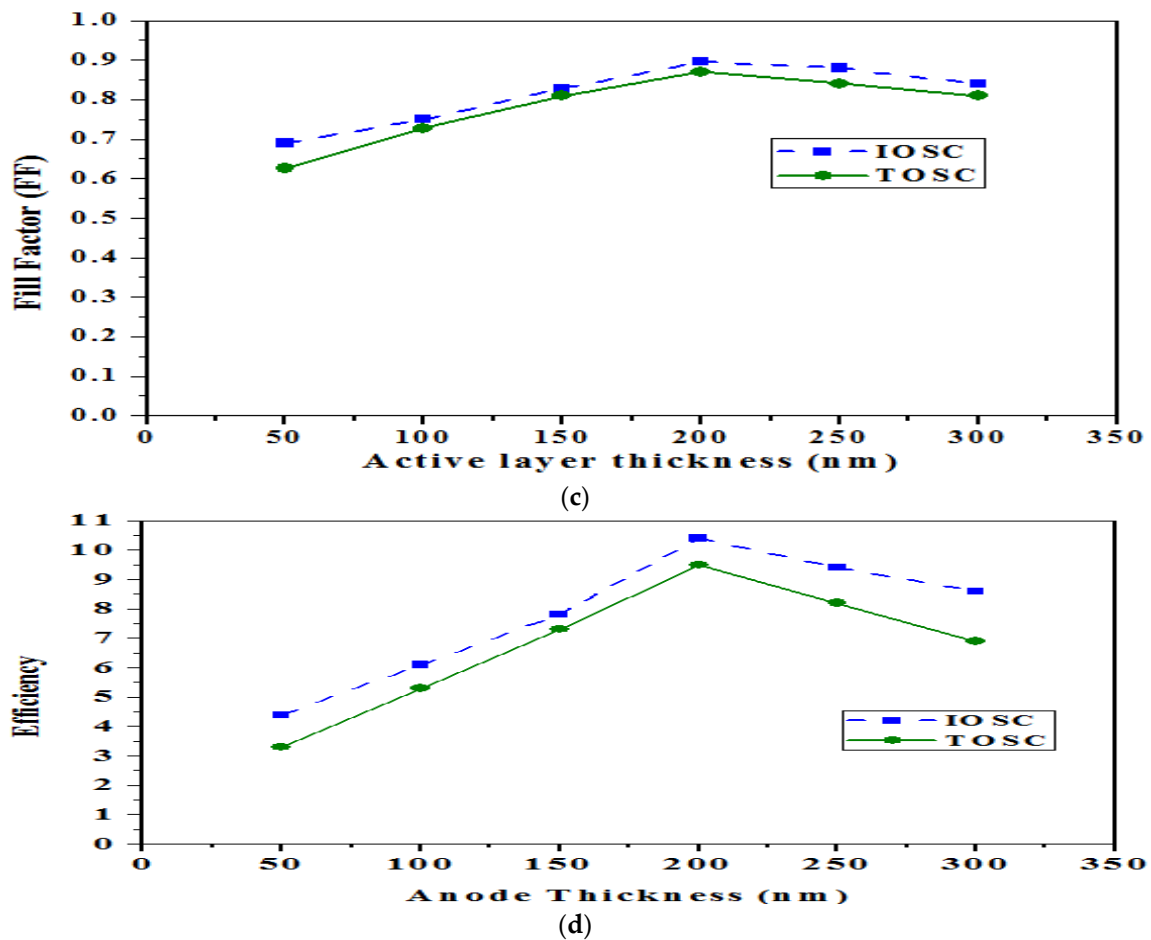


Figure 4. (a) J_{sc} , (b) V_{oc} , (c) FF, and (d) Efficiency. The output extracted (TOSC: Dashed lines and IO SC: Solid lines) for various active layer thicknesses is illustrated.

In the TOSC, the best thickness for J_{sc} is reached at around 200 nm, but in the IO SC, a saturation of the ideal J_{sc} is found at approximately 200 nm. If there is a peak in the current curve at a certain thickness, it indicates thinner thicknesses and the absorption is not complete. Significant thicknesses make it more difficult for excitons to get through and weaken the internal field that keeps them apart, thus carrier collection will be less efficient. The active layer thickness is due to interferences between layers caused by optical phenomena, such as reflections at layer boundaries and their interactions; the active layer thickness is critical when optimizing BHJ devices. Since the thickness of the active layer affects the absorption of light and, consequently, the formation of excitons inside the active layer, the analysis of the active layer thickness is critical. The TOSC and IO SC have thinner active layers, with the active layer of TOSC as 200 nm and IO SC as 200 nm. The higher active layer thickness is due to the series resistance effect, whereas V_{oc} drops marginally from 0.865 V in TOSC and IO SC to 0.89 V in both devices.

The V_{oc} value is solely determined by the differential between the donor HOMO and acceptor LUMO, and there is a slight change in V_{oc} by the active layer thickness. The V_{oc} increases as the active layer thickness grows in TOSC and IO SC BHJ NPD, as indicated in Figure 4b. In V_{oc} , there is no significant influence on active layer thickness fluctuation. When the applied bias voltage is zero, these values are produced. The connection between the number of excitons created and recombined during charge dissociation is represented by this value. The drop in J_{sc} indicates that the active layer's maximum number of excitons have recombined before reaching the p–n junction and that the recombination rate is complementary to J_{sc} . As a result, when the active layer thickness increases in TOSC and IO SC, the current density drops (thickness above 200 nm for TOSC and 200 nm for IO SC).

For both TOSC and IOSC, increasing the active layer thickness improves the current density (thickness from 50 to 200 nm for TOSC and 50 to 200 nm for IOSC). An increase in J_{sc} indicates that the active layer's maximal number of excitons reaches the electrodes and that the recombination rate is proportional to J_{sc} .

As illustrated in Figure 4c, in both TOSC and IOSC NPD, the fill factor decreases slightly when the active layer thickness increases over 200 nm. This demonstrates that as the width of the I-V characteristic curves increases, the maximum power obtained decreases. The FF in both TOSC and IOSC BHJ NPD will grow as the active layer thickness increases from 50 to 200 nm; while above 200 nm it starts fall. Figure 5 shows the simulation output extracted from the transfer matrix model for both the TOSC and IOSC structures for the active layer thickness of 200 nm. Figure 5a,b shows the photon density and absorbed photon density of the TOSC structure with the active layer thickness of 200 nm. Additionally, Figure 5c,d shows the photon density and absorbed photon density of the IOSC structure with the active layer thickness of 200 nm.

When TOSC and IOSC are compared, the J_{sc} of the IOSC is superior to the TOSC. This may be the case due to the light's transmission and absorption properties. Initially, light passes through ITO, then through HTL PEDOT/PSS, and through contact on the HTL side to the active layer. However, the converse is true in the second case. Light reaches the active layer via the material's n -component compact after passing through TiOx ETL [48–50]. Tunable White Light Transmission (TWFT) of the TiOx ETL is greater than the PEDOT/PSS HTL, which has lesser transparency to visible light than the PEDOT/PSS HTL 2.2 eV energy gap [51–54].

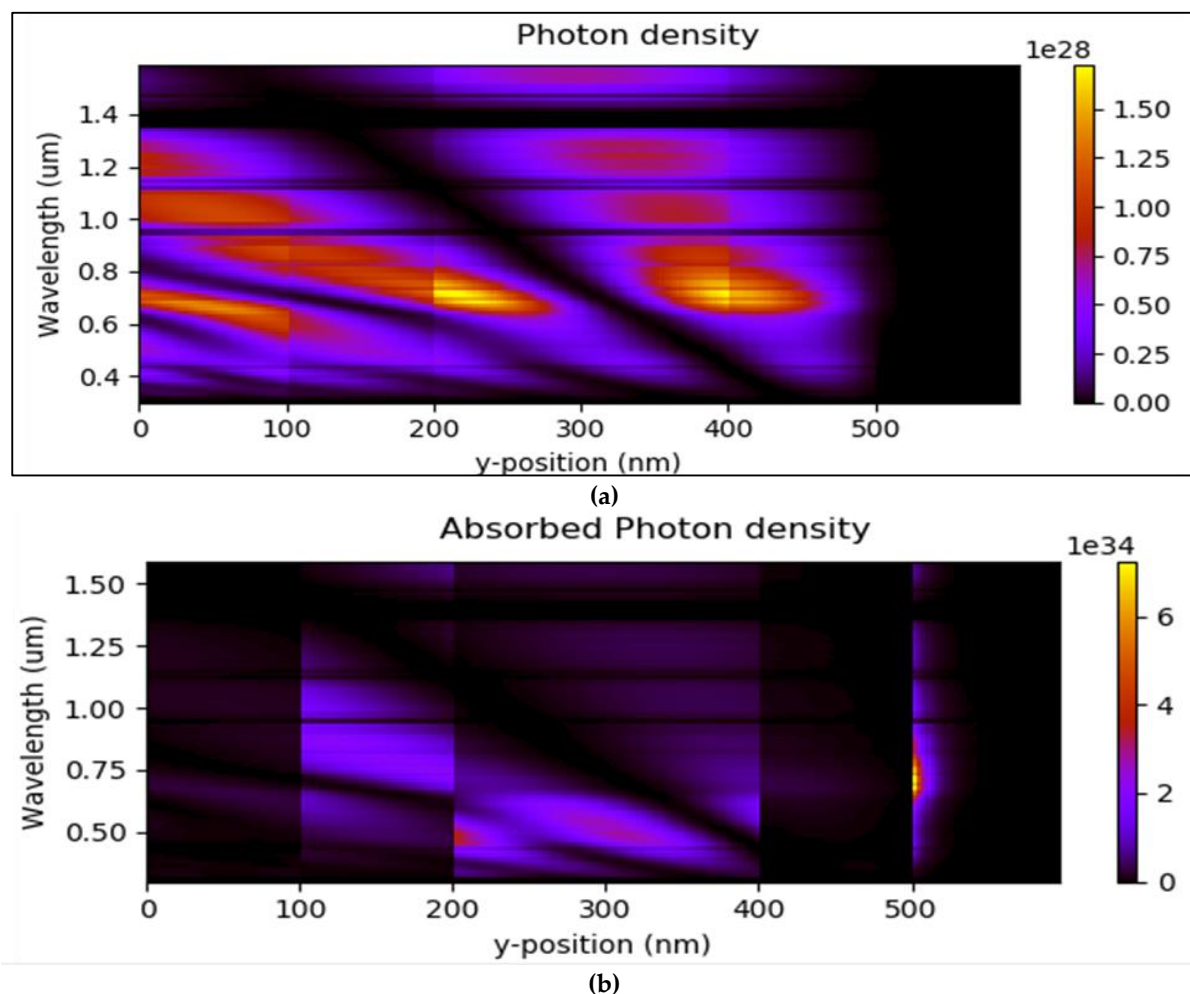


Figure 5. Cont.

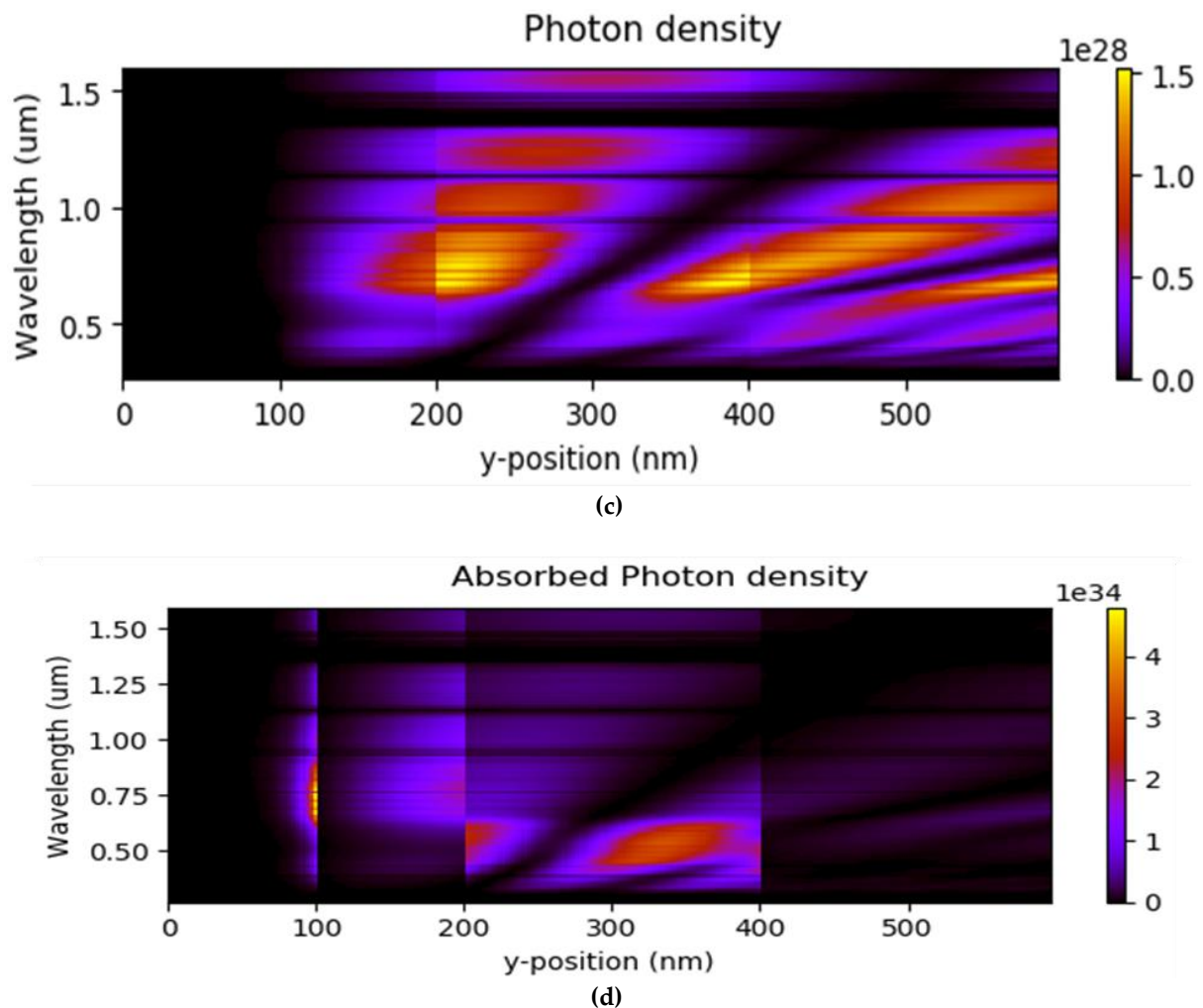


Figure 5. (a) Photon density of TOSC; (b) absorbed photon density TOSC; (c) photon density IOSC; (d) absorbed photon density IOSC. The output extracted using the transfer matrix method is illustrated.

4.2. Optimized Performance of TOSC and IOSC Using *s*-SWCNT:C₆₀ Active Layer

The results discussed above clearly demonstrated that IOSC BHJ NPD could provide superior performance than TOSC BHJ NPD devices for reasons elicited in the previous sections. The simulation results form the basis for the design of optimum geometries for the best performance. Of note, maximizing efficiency is the key to achieving the best possible performance. Table 1 shows the results of the foregoing analyses and comparison of results on different TOSC and IOSC NPD parameters, as well as the ideal active layer thicknesses for maximum performance. The best TOSC and IOSC performance parameters have been determined by running simulations with different parameters. The IOSC NPD device shows better results than TOSC NPD devices in all aspects. Figure 6 shows the J–V curve of the TOSC, IOSC, and a previously reported work [35] of 200 nm thickness of active layer.

Table 1. Optimum layer thicknesses for TOSC and IOSC NPD.

Parameter	TOSC	IOSC
Active layer thickness (nm)	200	200
Active layer material	<i>s</i> -SWCNT:C ₆₀	<i>s</i> -SWCNT:C ₆₀
V_{oc} (V)	0.865	0.89
J_{sc} (mA/cm ²)	15.46	18.02
η	9.5	10.4
FF%	87	89.5

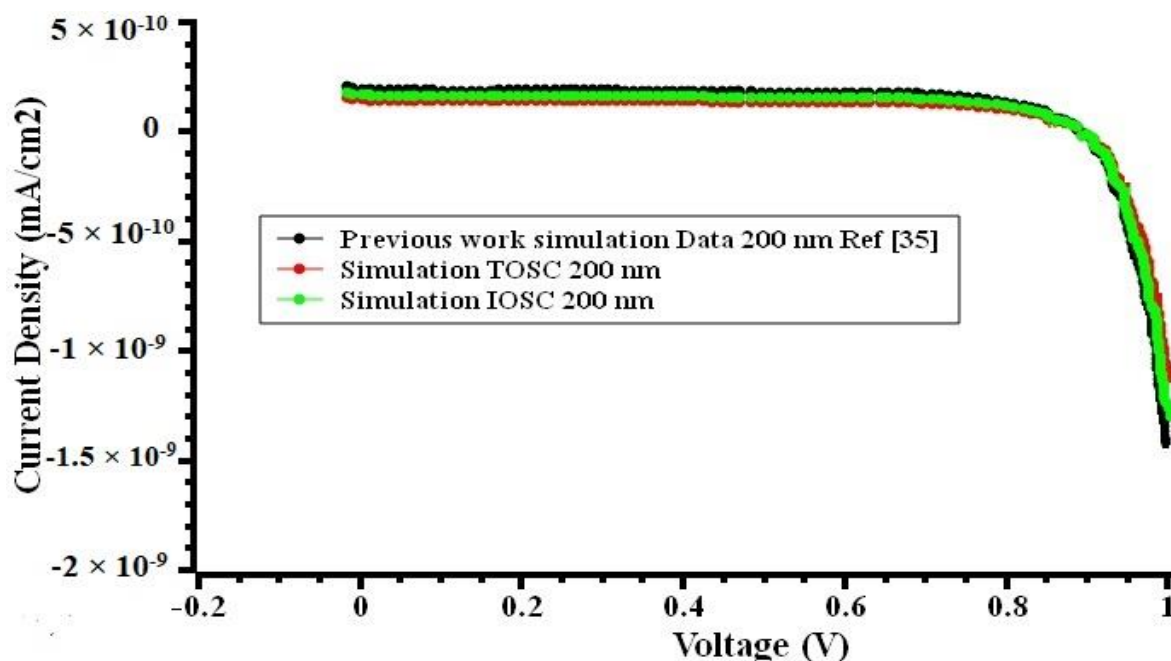


Figure 6. The J–V output plot of the IOSC (green line), TOSC (red line), and a previously reported work [35] (black line) of 200 nm thickness of active layer.

5. Conclusions and Future Recommendations

Traditional and inverted s-SWCNT:C₆₀ organic solar cells have been analyzed for enhanced performance. To design the TOSC and IOSC, a range of active layer thicknesses have been utilized. According to the findings, V_{oc} , J_{sc} , η , and FF were all evaluated and compared between TOSC and IOSC. In this research work, the active layer's thickness was varied to observe how it affected the results. In both TOSC and IOSC, the thickness of the active layer has an effect on the overall performance. As a consequence, the maximum efficiency for TOSC is attained by employing the ITO/PEDOT:PSS/s-SWCNT:C₆₀ (blended active layer)/TiOx/Al structure (efficiency of 9.5%). Another type of device (IOSC) has the most efficient structure, which was composed of ITO/TiOx/s-SWCNT:C₆₀ (blended active layer)/PEDOT:PSS/Al. This device has a top-to-bottom structure and an efficiency of 10.4%. With respect to the active layers, the s-SWCNT:C₆₀ displays the best power conversion efficiency, which was primarily attributed to its excellent optical and electrical characteristics, making it a strong contender in the role of the absorption layer.

This research proposes a viable way toward the effective deployment of OPV by adjusting their properties, which are heavily dependent on the results of organic solar cells to increase their efficiency. On the basis of the obtained data, it has been determined that the IOSC performance is superior to the TOSC in all categories. Finally, it has been concluded that IOSC NPD provides superior performance than TOSC.

In the future, this device will be optimized with fabrication using these nanomaterials. Thereafter, its characteristic will be verified with the simulated results. Moreover, the fabricated device has been implemented for future use in biomedical micro-device applications.

Author Contributions: V.M.M. conducted this research and wrote the article; V.M.M. designed and analyzed the model with data; V.M.S. verified the results and finalized the article. All authors have read and agreed to the published version of the manuscript.

Funding: This research received no external funding.

Institutional Review Board Statement: Not applicable.

Informed Consent Statement: Not applicable.

Data Availability Statement: All data and material used to prepare this manuscript are available in this document.

Conflicts of Interest: The authors declare no conflict of interest.

References

1. Ananthakumar, S.; Kumar, J.R.; Babu, S.M. Third-Generation Solar Cells: Concept, Materials and Performance—An Overview. *Emerg. Nanostructured Mater. Energy Environ. Sci.* **2019**, *23*, 305–339.
2. Li, Y.; Huang, X.; Ding, K.; Sheriff, H.K.M.; Ye, L.; Liu, H.; Li, C.Z.; Ade, H.; Forrest, S.R. Non-fullerene acceptor organic photovoltaics with intrinsic operational lifetimes over 30 years. *Nat. Commun.* **2021**, *12*, 1–9. [[CrossRef](#)] [[PubMed](#)]
3. Bernardo, G.; Lopes, T.; Lidzey, D.G.; Mendes, A. Progress in upscaling organic photovoltaic devices. *Adv. Energy Mater.* **2021**, *11*, 1–29. [[CrossRef](#)]
4. Williams, R. Becquerel photovoltaic effect in binary compounds. *J. Chem. Phys.* **1959**, *32*, 1505–1514. [[CrossRef](#)]
5. Loferski, J.J. The first forty years: A brief history of the modern photovoltaic age. *Prog. Photovolt. Res. Appl.* **1993**, *1*, 67–78. [[CrossRef](#)]
6. Goetzberger, A.; Hebling, C.; Schock, H.W. Photovoltaic materials, history, status and outlook. *Mater. Sci. Eng. R Rep.* **2003**, *40*, 1–46. [[CrossRef](#)]
7. Pillay, D.; Srivastava, V.M. Realization with fabrication of dual-gate MOSFET based source follower. *Silicon* **2022**, 1–11. [[CrossRef](#)]
8. Ohl, R.S. Light-Sensitive Electric Device. U.S. Patent 2402662, 25 June 1946.
9. Alferov, Z.I.; Andreev, V.M.; Kagan, M.B.; Protasov, I.I.; Trofim, V.G. Investigation of the influence of the AlAs-GaAs heterostructure parameters on the laser threshold current and the realization of continuous emission at room temperature. *Sov. Phys. Semicond.* **1971**, *4*, 1573–1575.
10. Chen, D.; Zhang, C.; Wang, Z.; Zhang, J.; Feng, Q.; Xu, S.; Zhou, X.; Hao, Y. Performance comparison of conventional and inverted organic bulk hetero-junction solar cells from optical and electrical aspects. *IEEE Trans. Electron Devices* **2013**, *60*, 451–457. [[CrossRef](#)]
11. Malti, I.; Chiali, A.; Sari, N.C. Numerical study of electrical behavior of P3HT/PCBM bulk hetero-junction solar cell. *Appl. Sol. Energy* **2016**, *52*, 122–127. [[CrossRef](#)]
12. Brabec, C.J. Organic photovoltaics: Technology and market. *Sol. Energy Mater. Sol. Cells* **2004**, *83*, 273–292. [[CrossRef](#)]
13. Yu, G.; Gao, J.; Hummelen, J.C.; Wudl, F.; Heeger, A.J. Polymer photovoltaic cells: Enhanced efficiencies via a network of internal donor-acceptor hetero-junctions. *Science* **1995**, *270*, 1789–1791. [[CrossRef](#)]
14. Scharber, M.C.; Sariciftci, N.S. Efficiency of bulk-heterojunction organic solar cells. *Prog. Polym. Sci.* **2013**, *38*, 1929–1940. [[CrossRef](#)] [[PubMed](#)]
15. Marinova, N.; Valero, S.; Delgado, J.L. Organic and perovskite solar cells: Working principles, materials and interfaces. *J. Colloid Interface Sci.* **2016**, *488*, 373–389. [[CrossRef](#)]
16. Kumavat, P.P.; Sonar, P.; Dalal, D.S. An overview on basics of organic and dye sensitized solar cells, their mechanism and recent improvements. *Renew. Sustain. Energy Rev.* **2017**, *78*, 1262–1287. [[CrossRef](#)]
17. Liang, Z.; Zhang, Q.; Jiang, L.; Cao, G. ZnO cathode buffer layers for inverted polymer solar cells. *Energy Environ. Sci.* **2015**, *8*, 3442–3476. [[CrossRef](#)]
18. Zhao, D.; Liu, P.; Sun, X.; Tan, S.; Ke, L.; Kyaw, A. An inverted organic solar cell with an ultrathin Ca electron-transporting layer and MoO₃ hole-transporting layer. *Appl. Phys. Lett.* **2009**, *95*, 153304. [[CrossRef](#)]
19. Zhao, D.; Tan, S.; Ke, L.; Liu, P.; Kyaw, A.; Sun, X.; Lo, G.; Kwong, D. Optimization of an inverted organic solar cell. *Sol. Energy Mater. Sol. Cells* **2010**, *94*, 985–991. [[CrossRef](#)]
20. Waldauf, C.; Morana, M.; Denk, P.; Schilinsky, P.; Coakley, K.; Choulis, S.; Brabec, C. Highly efficient inverted organic photovoltaics using solution based titanium oxide as electron selective contact. *Appl. Phys. Lett.* **2006**, *89*, 233517. [[CrossRef](#)]
21. White, M.S.; Olson, D.; Shaheen, S.; Kopidakis, N.; Ginley, D.S. Inverted bulk-heterojunction organic photovoltaic device using a solution-derived ZnO underlayer. *Appl. Phys. Lett.* **2006**, *89*, 143517. [[CrossRef](#)]
22. Zhang, F.; Xu, X.; Tang, W.; Zhang, J.; Zhuo, Z.; Wang, J.; Xu, Z.; Wang, Y. Recent development of the inverted configuration organic solar cells. *Sol. Energy Mater. Sol. Cells* **2011**, *95*, 1785–1799. [[CrossRef](#)]
23. Gilot, J.; Barbu, I.; Wienk, M.M.; Janssen, R.A. The use of ZnO as optical spacer in polymer solar cells: Theoretical and experimental study. *Appl. Phys. Lett.* **2007**, *91*, 113520. [[CrossRef](#)]
24. Behjat, A.; Torabi, N.; Dossthosseini, F. Improvement of light harvesting by inserting an optical spacer (ZnO) in polymer bulk hetero-junction solar cells: A theoretical and experimental study. *Int. J. Opt. Photonics* **2014**, *8*, 3–11.
25. Yang, C.; Zhang, C.; Chen, C.; Ren, Y.; Shen, H.; Tong, J.; Du, S.; Xia, Y.; Li, J. A new alcohol-soluble polymer PFN-ID as cathode interlayer to optimize performance of conventional polymer solar cells by increasing electron mobility. *Energy Technol.* **2022**, *10*, 2200199. [[CrossRef](#)]
26. Xue, L.; Liu, X.; Wang, Q.; Yang, M.; Du, S.; Yang, C.; Tong, J.; Xia, Y.; Li, J. Improved performance of organic solar cells by utilizing green non-halogen additive to modulate active layer morphology. *Energy Technol.* **2022**, 2200504. [[CrossRef](#)]

27. Ren, Y.; Liu, X.; Li, H.; Qin, J.; Du, S.; Lu, X.; Tong, J.; Yang, C.; Li, J. Utilizing non-conjugated small-molecular tetrasodium iminodisuccinate as electron transport layer enabled improving efficiency of organic solar cells. *Opt. Mater.* **2022**, *129*, 112520. [[CrossRef](#)]
28. Moorthy, V.M.; Rathnasami, J.D.; Pattan, A.S. Simulation and analysis of nano photo diode arrays using CNT's and graphene nano materials for sub-retinal implant. In Proceedings of the ISSS National Conference on MEMS, Smart Materials, Structures and Systems, Kanpur, India, 28–30 September 2016; pp. 1–8.
29. Moorthy, V.M.; Rathnasami, J.D.; Pattan, S. Comparison studies of planar and bulk hetero junction nano photo diodes using carbon nano tube's (CNT) and graphene for sub-retinal implant. In Proceedings of the IEEE Conference on Emerging Devices and Smart Systems–ICEDSS, Tiruchengode, India, 2–3 March 2018; pp. 197–202.
30. Moorthy, V.M.; Sugantharathnam, M.; Rathnasami, J.D.; Pattan, S. Design and characterization of graphene-based nano-photodiode array device for photo-stimulation of subretinal implant. *Micro Nano Lett.* **2019**, *14*, 1131–1135. [[CrossRef](#)]
31. Park, S.H.; Lee, S.J.; Lee, J.H.; Kal, J.; Hahn, J.; Kim, H.K. Large area roll-to-roll sputtering of transparent ITO/Ag/ITO cathodes for flexible inverted organic solar cell modules. *Org. Electron.* **2016**, *30*, 112–121. [[CrossRef](#)]
32. Lai, T.; Tsang, S.; Manders, J.; Chen, S.; Franky, S. Properties of interlayer for organic photovoltaic. *Mater. Today* **2013**, *16*, 424–432. [[CrossRef](#)]
33. Hu, L.; Song, J.; Yin, X.; Su, Z.; Li, Z. Research progress on polymer solar cell based on PEDOT: PSS electrodes. *Polymer* **2020**, *12*, 145. [[CrossRef](#)]
34. Dargar, S.K.; Srivastava, V.M. Analysis of short channel effects in multiple-gate (n,0)-Carbon Nanotube FETs. *J. Eng. Sci. Technol.* **2019**, *14*, 3282–3293.
35. Swapna, P.; Rao, Y.S. Simulation studies on semiconducting single walled carbon nanotube based bilayer and bulk hetero junction organic solar cells. In Proceedings of the 4th International Conference on Materials Processing and Characterization, Hyderabad, India, 14–15 February 2015; pp. 1634–1641.
36. Sariciftci, N.S.; Smilowitz, L.; Heeger, A.J.; Wudl, F. Photo induced electron transfer from a conducting polymer to buckminsterfullerene. *Science* **1992**, *258*, 1474–1476. [[CrossRef](#)] [[PubMed](#)]
37. Lee, J.K.; Coates, N.E.; Cho, S.; Cho, N.S.; Moses, D.; Bazan, G.C.; Lee, K.; Heeger, A.J. Efficacy of TiO_x optical spacer in bulk-heterojunction solar cells processed with 1, 8-octanedithiol. *Appl. Phys. Lett.* **2008**, *92*, 243308. [[CrossRef](#)]
38. Zhou, C.X.; Sun, J.X.; Deng, Z.J.; Zhou, S. Study of applicability of Boltzmann-statistics and two mobility models for organic semiconductors. *Semiconductors* **2013**, *47*, 1351–1357. [[CrossRef](#)]
39. Srivastava, V.M.; Singh, G. *MOSFET Technologies for Double-Pole Four Throw Radio Frequency Switch*; Springer International Publishing: Cham, Switzerland, 2014.
40. Zhou, T.C.; Chen, G.; Liao, R.J.; Xu, Z. Charge trapping and detrapping in polymeric materials: Trapping parameters. *J. Appl. Phys.* **2011**, *110*, 043724. [[CrossRef](#)]
41. Liu, N.; Chen, G. Changes in charge trapping/detrapping in polymeric materials and its relation with aging. In Proceedings of the IEEE Conference on Electrical Insulation and Dielectric Phenomena, Shenzhen, China, 20–23 October 2013; pp. 800–803.
42. Shi, X.H.; Sun, J.X.; Xiong, C.H.; Sun, L. Exponential-type density of states with clearly cutting tail for organic semiconductors. *Org. Electron.* **2016**, *30*, 60–66. [[CrossRef](#)]
43. MacKenzie, R.C.; Shuttle, C.G.; Chabiny, M.L.; Nelson, J. Extracting microscopic device parameters from transient photocurrent measurements of P3HT:PCBM solar cells. *Adv. Energy Mater.* **2012**, *2*, 662–669. [[CrossRef](#)]
44. Erray, M.; Hanine, M.; Boufounas, E.-M.; El Amrani, A. Combined effects of carriers charge mobility and electrodes work function on the performances of polymer/fullerene P3HT:PCBM based organic photovoltaic solar cell. *Eur. Phys. J. Appl. Phys.* **2018**, *82*, 1–14. [[CrossRef](#)]
45. Apaydin, D.H.; Yildiz, D.E.; Cirpan, A.; Toppare, L. Optimizing the organic solar cell efficiency: Role of the active layer thickness. *Sol. Energy Mater. Sol. Cells* **2013**, *113*, 100–105. [[CrossRef](#)]
46. Nam, Y.M.; Huh, J.; Jo, W.H. Optimization of thickness and morphology of active layer for high performance of bulk-heterojunction organic solar cells. *Sol. Energy Mater. Sol. Cells* **2010**, *94*, 1118–1124. [[CrossRef](#)]
47. Wang, X.; Sun, Q.; Gao, J.; Wang, J.; Xu, C.; Ma, X.; Zhang, F. Recent progress of organic photovoltaics with efficiency over 17%. *Energies* **2021**, *14*, 4200. [[CrossRef](#)]
48. Banerjee, S.; Gupta, S.K.; Singh, A.; Garg, A. Buffer layers in inverted organic solar cells and their impact on the interface and device characteristics: An experimental and modeling analysis. *Org. Electron.* **2016**, *37*, 228–238. [[CrossRef](#)]
49. Gowthaman, N.; Srivastava, V.M. Mathematical modeling of electron density arrangement in CSDG MOSFET: A nano-material approach. *J. Mater. Sci.* **2022**, *57*, 8381–8392. [[CrossRef](#)]
50. Xu, C.; Jin, K.; Xiao, Z.; Zhao, Z.; Ma, X.; Wang, X.; Li, J.; Xu, W.; Zhang, S.; Ding, L.; et al. Wind band-gap polymer with narrow photon harvesting in visible light range enable efficient semitransparent organic photovoltaics. *Adv. Funct. Mater.* **2021**, *32*, 2107934. [[CrossRef](#)]
51. Chang, S.Y.; Cheng, P.; Li, G.; Yang, Y. Transparent polymer photovoltaics for solar energy harvesting and beyond. *Joule* **2018**, *2*, 1039–1054. [[CrossRef](#)]
52. Weng, K.; Ye, L.; Zhu, L.; Xu, J.; Zhou, J.; Feng, X.; Lu, G.; Tan, S.; Liu, F.; Sun, Y. Optimized active layer morphology toward efficient and polymer batch insensitive organic solar cells. *Nat. Commun.* **2020**, *11*, 2855–2859. [[CrossRef](#)]

-
53. Borazan, I.; Altin, Y.; Demir, A.; Bedeloglu, A.C. Characterization of organic solar cells using semiconducting polymers with different band-gaps. *J. Polym. Eng.* **2019**, *39*, 636–641. [[CrossRef](#)]
 54. Luceno-Sanchez, J.A.; Diez-Pascual, A.M.; Capilla, R.P. Materials for photovoltaic: State of art and recent developments. *Int. J. Mol. Sci.* **2019**, *20*, 976. [[CrossRef](#)] [[PubMed](#)]